Temporal Dynamic Synchronous Functional Brain Network for Schizophrenia Classification and Lateralization Analysis

Cheng Zhu, Ying Tan, Shuqi Yang, Jiaqing Miao, Jiayi Zhu, Huan Huang, Dezhong Yao, and Cheng Luo

***Abstract*—Available evidence suggests that dynamic functional connectivity can capture time-varying abnormalities in brain activity in resting-state cerebral functional magnetic resonance imaging (rs-fMRI) data and has a natural advantage in uncovering mechanisms of abnormal brain activity in schizophrenia (SZ) patients. Hence, an advanced dynamic brain network analysis model called the temporal brain category graph convolutional network (Temporal-BCGCN) was employed. Firstly, a unique dynamic brain network analysis module, DSF-BrainNet, was designed to construct dynamic synchronization features. Subsequently, a revolutionary graph convolution method, TemporalConv, was proposed based on the synchronous temporal properties of features. Finally, the first modular test tool for abnormal hemispherical lateralization in deep learning based on rs-fMRI data, named CategoryPool, was proposed. This study was validated on COBRE and UCLA datasets and achieved 83.62% and 89.71% average accuracies, respectively, outperforming the baseline model and other state-of-the-art methods. The ablation results also demonstrate the advantages of TemporalConv over the traditional edge feature graph convolution approach and the improvement of CategoryPool over the classical graph pooling approach. Interestingly, this study showed that the lower-order perceptual system and higher-order network regions in the left hemisphere are more severely dysfunctional than in the right hemisphere in SZ, reaffirmings the importance of the left medial superior frontal gyrus in SZ. Our code was available at: https://github.com/swfen/Temporal-BCGCN.**

***Index Terms*—Dynamic functional connectivity, graph pooling, hemispherical lateralization, rs-fMRI, schizophrenia, temporal graph convolution.**

I. INTRODUCTION

Currently, artificial intelligence methods that assist in diagnosing schizophrenia (SZ) are a critical research focus in the field of clinical medicine for psychiatric disorders [1-3]. Severe behavioral dysfunction is common among SZ patients, with a lifetime prevalence of approximately 1% [4] and a shorter life expectancy of about 15 years compared with the general population [5]. Concurrently, the diagnosis and treatment of SZ are arduous because a wide range of brain dysfunctions, in perception, thinking, emotion, and behavior, are involved. Resting-state functional magnetic resonance imaging (rs-fMRI) [6], is a non-invasive medical imaging technique that measures fluctuations of blood oxygen level (BOLD) signals in various regions of interest (ROIs) of the brain. The rs-fMRI has been used to study abnormal functional connectivity patterns in SZ patients [7-12]. Although previous studies have used computerized methods to analyze rs-fMRI data, there are still some difficulties in the development of computer-aided diagnostic techniques for SZ. They include problems in utilizing rs-fMRI data to the maximum extent to construct complex brain networks, better extracting features from the networks, and further exploring potential functional anomalies in the brains of individuals with SZ.

The activity of nodes and connectivity patterns in the brain network change over time [13], posing challenges in understanding advanced cognitive abnormalities in patients with psychiatric illnesses. Existing studies have shown that brain activity is always in a dynamic pattern of neural activity, and it is believed that dynamic functional connectivity (dFC) analysis can reveal temporal dynamics changes masked by static functional connectivity (sFC) [14, 15]. Therefore, the use of dFC to describe the state of brain network activity has attracted research interest in the classification and analysis of psychiatric disorders [16-20]. The dFC analysis uses a sliding window to slice the rs-fMRI data into multiple time segments, providing a new way to explore the dynamic mechanisms of brain activity further. Lin *et al.* [21] proposed a convolutional recurrent neural network (CRNN) for extracting high-level features of the dFC network and implementing classification. Ramirez-Mahaluf *et al.* [22] found a temporal disorganization of dFC in the brains of patients with first-episode psychosis. Most studies have explored the dynamic patterns of change in brain networks using the dFC mechanisms but have not fully

This work was supported by a grant from the STI 2030-Major Projects (2022ZD0208500), the open fund of state key laboratory of Pharmaceutical Biotechnology (KF-202204), the National Natural Science Foundation of China (61933003, U2033271, 82074003, 82174083), Chinese medicine (ethnic medicine) frontier research and development innovation team of Sichuan Administration of Traditional Chinese Medicine(No. 2022C010), the Sichuan Provincial Program of Traditional Chinese Medicine of China (2024ZD014), and the Fundamental Research Funds for the Central Universities of China, Southwest Minzu University (ZYN2023098). (Cheng Zhu and Shuqi Yang contributed equally to this work.) (Corresponding author: Ying Tan, Jiaqing Miao, Cheng Luo).

Cheng Zhu, Ying Tan, Shuqi Yang, Jiaqing Miao, Jiayi Zhu are with The Key Laboratory for Computer Systems of State Ethnic Affairs Commission, Southwest Minzu University, Chengdu, China. (e-mail: 190852112021@stu.swun.edu.cn; ty7499@swun.edu.cn; yangshuqi@stu.swun.edu.cn; jiaqing_miao@swun.edu.cn; zhujiayii0102@163.com).

Huan Huang, Cheng Luo, Dezhong Yao are with MOE Key Lab for Neuroinformation, High-Field Magnetic Resonance Brain Imaging Key Laboratory of Sichuan Province, The Clinical Hospital of Chengdu Brain Science Institute, University of Electronic Science and Technology of China, Chengdu 611731, China. (e-mail: huan_huang17@163.com; chengluo@uestc.edu.cn; dyao@uestc.edu.cn).

mined the implied synchronization trends between brain regions.

Graph neural networks (GNNs) extend deep learning (DL) methods to non-Euclidean domains to extract and aggregate feature information in graph-structured data more effectively, showing superior performance in the SZ classification. Lei *et al.* [23] used a graph convolutional network (GCN) to extract features from rs-fMRI data to reveal abstract and complex relationships within brain networks and identify topological abnormalities in the functional networks of SZ patients. Chang *et al.* [24] applied a GNN to learn the topology of brain networks in the source space to better capture the complex relationships involved in the mismatch negativity (electrophysiological indicator) in the electroencephalography of SZ patients. In this study, we found that most of the edge vector graph convolution methods, represented by Edge-Conditioned Convolution (ECConv) [25], disrupt the temporal construction of node and edge features during the convolution of traditional GNNs when applied to brain time series data. This disruption may degrade the classification performance of the model.

Some studies have found that SZ patients may have hemispheric lateralization abnormalities [7,26] and disruptions to the mutual coordination of left and right hemisphere functions of the brain [27, 28]. Owing to the essential role of pooling operations in the network structure, the use of pooling to verify brain lateralization abnormalities in SZ patients has become a topic of research interest. To further exploit the latent relationships among nodes, some studies clustered the nodes during pooling and then selected the nodes based on class clusters, where the selection was often data-driven. Yuan *et al.* [29] proposed a graph pooling technique that assigns nodes with similar features to the same class clusters and uses them for the prediction task of the graph structure. Gopinath *et al.* [30] introduced a learnable pooling strategy with a difference pooling technique to split the network into two separate paths, one for computing the latent features of nodes and the other for clustering the features into node class clusters. However, to verify the presence of abnormal lateralization in SZ patients, it is often necessary to divide the brain regions in the left and right hemispheres into two clusters according to prior knowledge. Existing graph clustering pooling strategies are limited in this case as they cannot target potential functional abnormalities in the left and right hemispheres of SZ patients.

To address these limitations, an advanced GCN improvement model based on dynamic brain network analysis, the temporal brain category graph convolutional network (Temporal-BCGCN), was proposed. Firstly, the dynamic synchronous functional brain network (DSF-BrainNet) with temporal dynamic synchronous properties was built using a sliding window technique to obtain information about nodes in brain regions and the interrelationships between nodes. Secondly, the proposed TemporalConv enables the convolution process to adapt to the dynamic synchronization rule in DSF-BrainNet. Finally, the pooling strategy CategoryPool was employed in the pooling layer of GCN to improve the accuracy of SZ classification and investigate further hemispheric lateralization abnormalities in SZ patients.

The main contributions of this paper can be summarized as follows:

1) A unique dynamic brain network analysis module, DSF-BrainNet, is proposed. DSF-BrainNet brings new perspectives for understanding further the dynamic fluctuation patterns of various brain regions over time. This module was used as the input for the GCN.

2) A revolutionary convolutional method called TemporalConv is presented. TemporalConv convolves the features of the rs-fMRI data obtained from each time slice independently. The original concept of temporal convolution provides a new reference for subsequent researchers performing graph convolution on rs-fMRI and other temporal data.

3) A novel pooling strategy called CategoryPool is proposed. In rs-fMRI research, CategoryPool is the first modular hemispheric lateralization abnormalities test tool used for DL. This method has strong generalization and can be transferred to other medical research fields.

II. DATASETS AND PREPROCESSING

Two public datasets were selected for model evaluation, ablation and lateralization analysis in this study: the Center for Biomedical Research Excellence (COBRE) dataset [31] and the University of California Los Angeles (UCLA) dataset [32], with the following sources and corresponding preprocessing.

The COBRE dataset was obtained from the Center for Biomedical Research Excellence, which selected rs-fMRI images of 112 subjects as data, including 48 SZ patients and 64 healthy controls (HC). Informed consent was obtained from each subject in accordance with the COBRE Office of Human Research Protections. The UCLA dataset was obtained from the UCLA Consortium for Neuropsychiatric Phenomics LA5c Study, which selected rs-fMRI images of 80 subjects as data, including 41 SZ patients and 39 HC. All subjects gave written informed consent in accordance with procedures approved by the UCLA Institutional Review Board. In addition, subjects with a diagnosis of a neurological disorder, mental retardation, severe head trauma, substance abuse, or dependence within the previous 12 and six months were excluded from the aforementioned two datasets, respectively.

The preprocessing of resting-state functional data was performed using the DPABI toolbox [33]. The first 10 volumes were removed for signal equilibrium and allowed the participants to adapt to the scanning noise. The preprocessing pipeline included the following steps: (1) Slice-time correction (to correct for temporal shifts of different slices). (2) Realignment to the mean functional image using a trilinear interpolation with degrees of freedom. (3) Normalization to the standard EPI template and resampling to $3 \times 3 \times 3$ mm^3 voxels. (4) Nuisance signals were regressed out, including the linear trend, 24-parameter motion correction, mean white matter, and cerebrospinal fluid signals. The 24 motion parameters included six rigid-body motion parameters (x, y, and z translations and rotations) and their values at the previous time point and the 12 corresponding squared values [34]. The global signal was not regressed because a recent excellent study demonstrated that an altered global brain signal was observed in patients with schizophrenia, which may underlie profound alterations in the

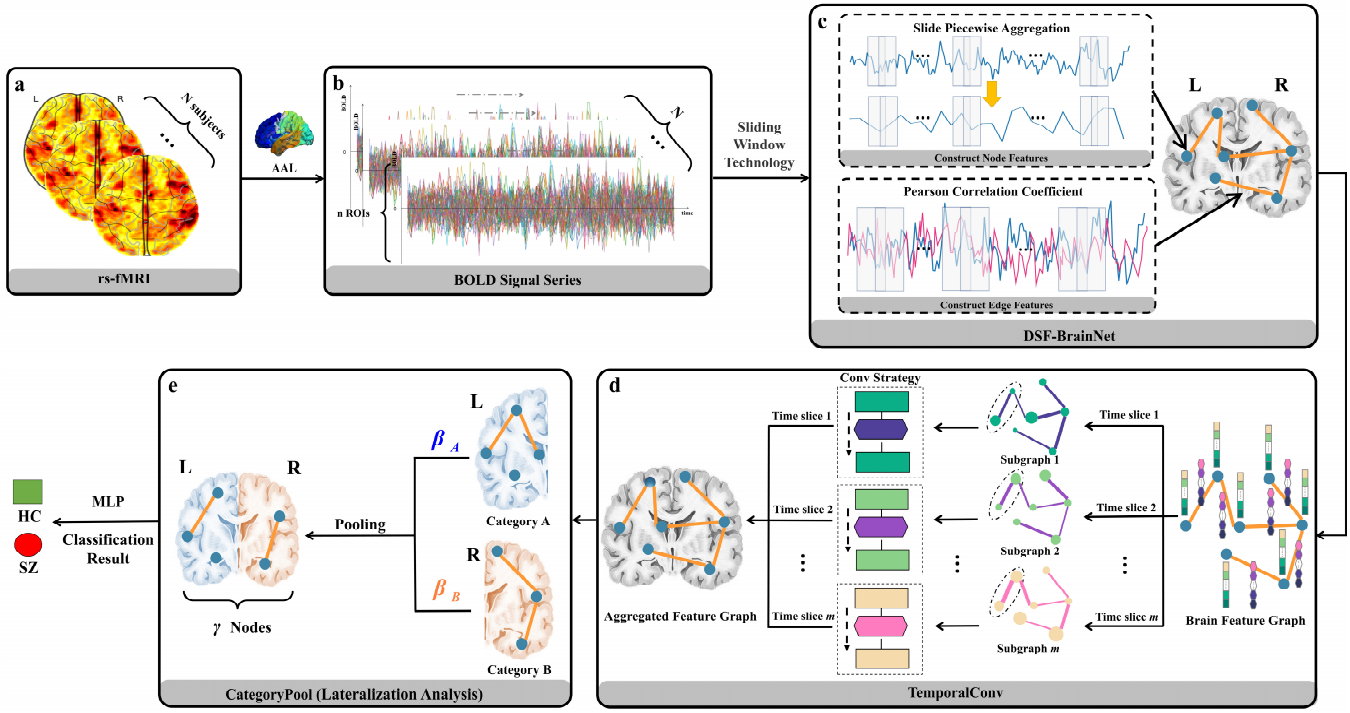

Fig. 1. Overall flowchart of the Temporal-BCGCN Architecture. (a) rs-fMRI. (b) BOLD Signal Series. (c) DSF-BrainNet. (d) TemporalConv. (e) CategoryPool.

neural information flow in patients with SZ, regressing out the global mean signal can distort between-group comparisons of inter-regional correlation [35]. (5) After removing the potentially confound signals using averaged brain tissue time series and estimated head motion signals in the multiple regression model, the residuals were band-pass filtered (0.01–0.08 Hz) to further suppress low-frequency drifts and physiological noises such as breathing and heartbeat. (6) They were smoothed using a Gaussian kernel (FWHM = 8 mm). Finally, dimensionality reduction was implemented by parcellating the brain into 90 functionally defined ROIs from the automated anatomical labeling (AAL-90) [36] atlas, extracting the smoothed BOLD time series from these regions.

III. METHODS

A. Overview of Temporal-BCGCN Architecture

In this study, an advanced Temporal-BCGCN model was proposed for classification and brain function lateralization analysis of SZ patients. The structural framework is illustrated in Fig. 1.

Fig. 1(a) shows the brain rs-fMRI data of N subjects. The brain data of N subjects are entered into the AAL template, and each subject is given the corresponding BOLD signal on each of the n ROIs to obtain the N sets of datasets in (b), where each set contains the BOLD signal sequence of the n ROIs. The horizontal coordinates of the BOLD signal in Fig. 1(b) represent the time variation, the vertical coordinates represent the BOLD signal values, and the oscillating dashes in each color represent the specific BOLD signal values for each ROI at the corresponding time points. The BOLD signal in Fig. 1(b) is processed using a sliding window technique to obtain the time slices in Fig. 1 (c), and the node features and edge features are calculated for each time slice. In particular, in Fig. 1(c), we propose the DSF-BrainNet module to construct a temporally synchronized feature brain network. First, we used the sliding window technique to divide the temporal signals of each subject into partially overlapping time slices. Then the signals of ROIs within each time slice were analyzed using the slide piecewise aggregation (SPA) technique to construct the graph node features. The Pearson correlation coefficient (PCC) between two ROIs within each time slice was calculated to construct the graph edge features. Using a graph node as an example, the feature values computed for each time slice represent the individual components of the feature vector associated with that node. The entire feature vector is constructed by concatenating these components in a chronological sequence. The process of constructing the edge features follows a procedure similar to that described above. (For specific details, refer to Section III.B.1 or III.B.2). Subsequently, the brain feature graphs constructed in Fig. 1(c) were fed into Fig. 1(d), the TemporalConv operation. We set up m independent convolution paths according to the number of time slices such that nodes and edge features under different time slices were signaled in independent paths, ensuring that the synchronous timing properties in DSF-BrainNet were not destroyed during the convolution process. In addition, the convolution module was run twice in succession. The aggregated feature graphs obtained in Fig. 1(d) were then fed into Fig. 1(e), where the left and right hemisphere nodes were set to Categories A and B, respectively. After determining the total number of nodes γ to be retained in the pooling, the corresponding abnormal

propensity parameters β_A and β_B were set to control the proportion of nodes retained in the left and right hemispheres, respectively. Finally, the pooled brain maps were fed into the multi-layer perceptron (MLP) to obtain the classification results. The optimal model values of β_A and β_B were determined through multiple experiments for further lateralization analysis.

B. DSF-BrainNet

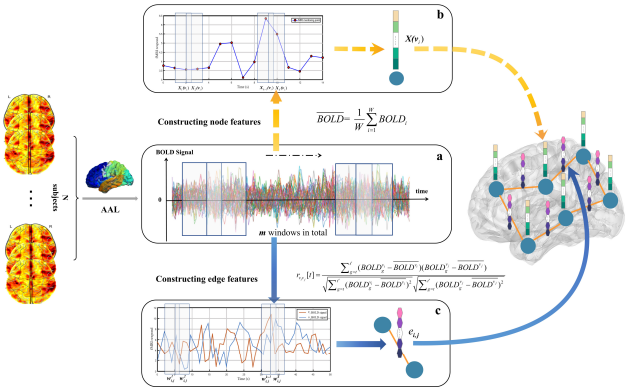

Fig. 2. Flow of DSF-BrainNet method. (a) Using the sliding window technique, the time series is sequentially divided into different time slices, (b) Using the SPA method, the node feature information under each time slice is constructed synchronously, (c) Using PCC, the constructed edge feature information under each time slice.

DSF-BrainNet is the feature graph structure that needs to be fed into the GCN model. DSF-BrainNet is topologically composed of graph nodes and edge features. To reflect the fluctuation of brain activity over time, the graph nodes and edge features are organized as time series data, and they maintain a time-based synchronization property. They are defined as follows: $G=(V,E)$ denotes the undirected complete graph, where $V=\{v_1,v_2,\cdots,v_n\}$ denotes the set of brain region nodes, and n denotes the number of nodes, that is, the number of ROIs. Similarly, $E=\{(v_i,v_j)\}$ denotes the set of edges between nodes in the graph, where $v_i,v_j\in V$. As E contains M elements, there are $M=C_n^2$ edges in the graph. Therefore, a function $X:V\mapsto\mathbb{R}^m$ assigns features to each node and a function $L:E\mapsto\mathbb{R}^m$ assigns features to each edge. Here, m denotes the length of the node feature vector, that is, the number of time slices. Therefore, $X(v_i)\in\mathbb{R}^m, i=1,2,\cdots,n$ is the feature vector of node v_i. $X_k(v_i), k=1,2,\cdots,m$ represents the feature component of $X(v_i)$ in the k^{th} time slice. $L(v_i,v_j)\in\mathbb{R}^m$ is the edge feature vector between nodes v_i,v_j. $L_k(v_i,v_j), i\neq j$ represents the feature component of $L(v_i,v_j)$ in the k^{th} time slice.

For a node v_i, the set of its neighboring nodes is defined as $Ne(v_i)$, that is,

$$Ne(v_i)=\left\{v_j\middle|(v_i,v_j)\in E\right\}, \tag{1}$$

where v_j denotes the neighboring nodes of v_i.

In Fig. 2, the rs-fMRI data of the N subjects are shown on the leftmost side. The brain structure of each subject was divided into 90 ROIs using an AAL-90 template. Thus, for each subject, the rs-fMRI data correspond to the BOLD signals of 90 ROIs. In Fig. 2(a), the entire scan time is divided into m time slices using the sliding window technique, and the acquired time slices are then input into Fig. 2(b) and Fig. 2(c). Subsequently, node and edge features are constructed for the BOLD signals within each time slice using the corresponding methods. Finally, all node and edge features form a DSF-BrainNet.

1) Sliding window technique

As a classical feature acquisition method, the sliding window technique has been widely applied to solve practical problems in various fields [37-39]. Therefore, in this study, sliding windows were used to construct node and edge features to exploit fully the temporal information in the rs-fMRI data. Taking the rs-fMRI brain data of a subject as an example, a reasonable window width W and sliding step s were chosen for a time series of length K. The entire time series was divided into m time slices by shifting the sliding window over the time series K with a given sliding step s. The starting point of each time slice was $t\in[0,K-W]$ and the ending point was $t'=t+W$. It should be emphasized that t can only be an integer. Therefore, the total number of time slices m could calculated using

$$m=\left\lceil\frac{K-W}{s}\right\rceil+1, \tag{2}$$

where $\lceil\ \rceil$ denotes the ceiling function.

2) Calculation of node features using SPA method

Because rs-fMRI is a time series consisting of multiple discrete signal points, this study extended the piecewise aggregation approximation method by applying a continuous time series to the rs-fMRI discrete time series and proposed the SPA method. After data reduction, the rs-fMRI data were organized into graph-node features.

Specifically, taking the rs-fMRI signal of any brain region in a subject, the specific mathematical procedure of SPA can be expressed as follows. In node v_i, the signal values $BOLD^{v_i}\in\mathbb{R}^W$ obtained in each time slice are averaged to obtain $\overline{BOLD^{v_i}}=\frac{1}{W}\sum_{i=1}^{W}BOLD_i^{v_i}$, where $BOLD_i^{v_i}$ denotes the i^{th} component of $BOLD^{v_i}$. In total, m BOLD signals are generated for each brain region in m time slices, and nodal feature vectors are obtained by connecting them in time order.

3) Calculation of edge features using PCC

In this study, a sliding window was used to construct dFC. Considering nodes v_i and v_j as an example, the PCC was used to calculate the edge feature components $L_k(v_i,v_j)$ of v_i and v_j under the k^{th} time slice. Subsequently, the correlation coefficients under all the time slices were arranged to form the edge feature vector $L(v_i,v_j)$. Specifically, the component $L_k(v_i,v_j)$, i.e., the correlation coefficient $r_{v_iv_j}[k]$ $(-1<r<1)$,

was calculated for the k^{th} time slice, as shown in Eq. (3):

$$r_{v_i v_j}[k] = \sum_{g=t}^{t'} (BOLD_g^{v_i} - \overline{BOLD^{v_i}})(BOLD_g^{v_j} - \overline{BOLD^{v_j}}) \Big/ \sqrt{\sum_{g=t}^{t'} (BOLD_g^{v_i} - \overline{BOLD^{v_i}})^2} \sqrt{\sum_{g=t}^{t'} (BOLD_g^{v_j} - \overline{BOLD^{v_j}})^2}, \quad (3)$$

where $BOLD_g^{v_i}$ and $BOLD_g^{v_j}$ represent the signal values of v_i and v_j, respectively at the time point g. $\overline{BOLD^{v_i}}$ and $\overline{BOLD^{v_j}}$ represent the corresponding mean signal value in the current time slice. Using the sliding window technique, a total of m correlation coefficients are generated under m time slices. Subsequently, Min–Max Normalization is employed to scale the PCC values within the range of 0 to 1. The above m PCCs are used to construct $L(v_i, v_j)$. The specific forms are given by Eq. (4):

$$L(v_i, v_j) = \left\{ r_{v_i v_j}[1], r_{v_i v_j}[2], \cdots, r_{v_i v_j}[m] \right\}^T \in \mathbb{R}^m \quad (4)$$

C. TemporalConv

TemporalConv ensures that the temporal dynamic structure of features is not destroyed during convolution. Most graph convolution methods cannot handle multi-dimensional edge feature vectors. Those that can handle them mostly make use of fully connected operation, i.e., transforming the dimensionality of the edge feature vectors to match the node dimensionality through a linear layer (multiple linear layers form an MLP in ECConv), such as in GATConv [40] and UniMPConv [41]. Because the fully connected approach for DSF-BrainNet destroys the temporal synchronization between features, this study improved on the traditional edge convolution approach represented by ECConv by proposing TemporalConv.

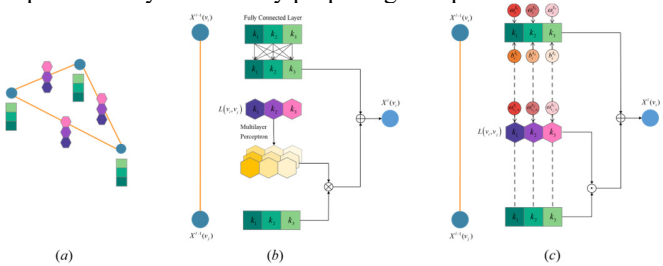

Fig. 3. Comparison of ECConv and TemporalConv convolution processes: (a) Schematic diagram of DSF-BrainNet. (b) Convolution process of applying ECConv to DSF-BrainNet. (c) Convolution process of applying TemporalConv to DSF-BrainNet.

In Fig. 3(a), the green gradient bars represent the node feature vectors and the purple gradient blocks represent the edge feature vectors, Fig. 3(b) shows the use of the ECConv method for the DSF-BrainNet constructed in this study, where $\otimes$ represents matrix multiplication; $\oplus$ represents element-wise addition; Assuming the total number of time slices is 3, then k_1, k_2, k_3 represents different time slices or pathways of the feature vectors, and it is assumed that $l \in \{0,1,\cdots,l_{\max}\}$ is the layer index in a feed-forward neural network. Specifically, for the target node feature $X^{l-1}(v_i) \in \mathbb{R}^m$ to be convolved, ECConv uses an MLP to transform the adjacent edge feature $L(v_i, v_j) \in \mathbb{R}^m$ into the matrix $\mathbb{R}^{m \times m}$. Thereafter matrix multiplication is performed between the adjusted matrix and the corresponding adjacent node feature vectors $X^{l-1}(v_j)$. Finally, the result is added element-wise to the self-connected target node $X^{l-1}(v_i)$ to obtain the convolved target node $X^l(v_i)$. However, the fully connected operation in MLP and self-connection destroy the synchronous timing relationship of features; therefore, the ECConv method is not suitable for the data organization form of this study. Fig. 3(c) represents the application of TemporalConv to the DSF-BrainNet constructed in this study, where $\odot$ represents the element-wise product. Specifically, in this convolution process, each graph node in each time slice forms an independent convolution path with its neighboring nodes and edges to ensure that the features of the convolved graph nodes remain in temporal order. Further, unlike ECConv where all edge vectors share a single learnable weight in the MLP, TemporalConv sets a unique adaptive weight for each edge feature component in each time slice to facilitate the importance of all edge feature components in all time slices. This information transfer process is bidirectional as the nodes in the graph are neighbors of each other. The independent convolution process for each time slice is represented by the gray dashed line in Fig. 3. In summary, TemporalConv preserves the temporal synchronization of features better than ECConv in the convolution process.

As in the notation presented in Section III.B, there exists function relation $X^l : V \mapsto \mathbb{R}^{d_l}$ to assign features to each graph node, and function relation $L^l : E \mapsto \mathbb{R}^{d_l}$ to assign features to each edge, where d_l is the feature dimension of the nodes and edge feature vectors of the l^{th} layer of the neural network. Simultaneously, let $k \in \{k_1, k_2 ..., k_{d_l}\}$ be the independent convolution pathway of each time slice in TemporalConv. It should be emphasized that the feature dimension of any node and edge in each time slice is one. Therefore, taking the k^{th} pathway in a time slice as an example, its convolved node feature value $X_k^l(v_i)$ is the sum of two parts. The first part is $X_k^{l-1}(v_i)$ under the influence of the adaptive weight parameter ω_i^k, and learnable bias parameter b_i^k, and the second part is the sum of all adjacent edge feature values $L_k^{l-1}(v_j, v_i)$ of the node and the corresponding adjacent node feature values $X_k^{l-1}(v_j)$ under the influence of the adaptive weight ω_{v_i, v_j}^k, where $v_j \in Ne(v_i)$. Therefore, the TemporalConv calculation process under the k pathway is as follows:

$$X_k^l(v_i) = \omega_i^k X_k^{l-1}(v_i) + b_i^k + \sum_{v_j \in Ne(v_i)} \omega_{v_j, v_i}^k L_k^{l-1}(v_j, v_i) X_k^{l-1}(v_j) \quad (5)$$

In addition, for a graph structure constructed without edge features, Eq. (5) can be simplified as follows:

$$X_k^l(v_i) = \omega_i^k X_k^{l-1}(v_i) + b_i^k + \sum_{v_j \in Ne(v_i)} \omega_{v_j, v_i}^k X_k^{l-1}(v_j) \quad (6)$$

D. CategoryPool

To improve further the classification accuracy of SZ patients and analyze hemispheric lateralization abnormalities, we proposed CategoryPool. As shown in Fig. 4, this method divides the brain nodes into two categories: left and right hemispheres. After determining the total number of nodes γ to be retained, the proportion of brain regions to be retained in these two categories (β_A , β_B) was set to investigate the effect of different retention ratios on the classification accuracy of SZ patients. Additionally, various node scoring strategies can be nested in CategoryPool pooling to filter the reserved nodes; this method mainly adopts the node scoring strategy of Top-k [42] for experimental exploration.

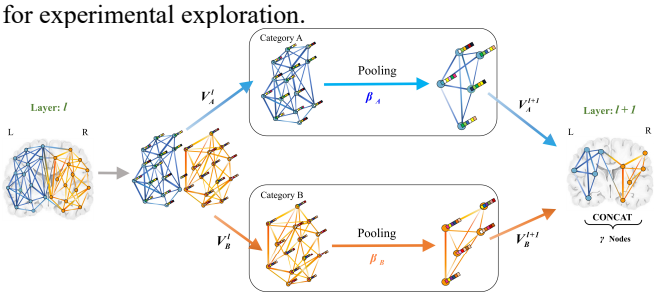

Fig. 4. CategoryPool Process Diagram.

In Fig. 4, the set of brain nodes V^l of the l^{th} layer neural network is firstly divided into two categories: left hemisphere V_A^l and right hemisphere V_B^l. Secondly, intra-class pooling of nodes within the two classes using propensity parameters β_A, β_B respectively, is performed. In particular, the nodes in V_A^l and V_B^l are firstly scored and ranked adaptively and then the top $\beta_A\gamma$ and $\beta_B\gamma$ brain regions in V_A^l and V_B^l are extracted to form node sets V_A^{l+1} and V_B^{l+1} in the $l+1^{th}$ layer, respectively. Finally, the pooled γ nodes are regrouped back into the GCN for output. Notably, $\beta_A\gamma+\beta_B\gamma=\gamma$.

Taking the brain graph of a subject as an example, $V^l=\{v_1,v_2,\cdots,v_n\}$ denotes the set of ROIs and n denotes the number of ROIs. Then, all ROIs were divided into two categories: V_A and V_B in the left and right hemispheres, according to the AAL template, which can be denoted as

$$\begin{aligned} V_A^l&=[v_1^A,v_2^A,\cdots,v_{n_A}^A] \\ V_B^l&=[v_1^B,v_2^B,\cdots,v_{n_B}^B] \end{aligned}, \tag{7}$$

where A and B indicate the left and right hemisphere nodes, respectively. n_A and n_B denote the numbers of nodes in V_A^l and V_B^l, respectively, and $n_A+n_B=n$. Here, a propensity parameter β_i is defined, where $0<\beta_i<1, i=A\ or\ B$. Then, $\beta_A\gamma$ and $\beta_B\gamma$ are the numbers of brain regions to be reserved for the left and right hemisphere nodes, respectively.

Finally, we feed V_A^l and V_B^l into separate Top-k pooling kernels. In the Top-kPool, adaptive scores are computed for all nodes (with varying computation methods for different graph pooling kernels), followed by ranking based on these scores, and selecting the top $\beta_A\gamma$ and $\beta_B\gamma$ nodes for retention. The node score calculation formula is as follows:

$$score(v_i)=\frac{X^l(v_i)\otimes p}{\|p\|_2}, \tag{8}$$

where $X^l(v_i)\in\mathbb{R}^{1\times d_l}$ is obtained from the node features after message passing by the convolution module; $p\in\mathbb{R}^{d_l\times 1}$ denotes the learnable projection vector; $\otimes$ denotes matrix multiplication; and $\|\cdot\|_2$ denotes the Euclidean distance (L_2 norm). Further, we sort the raw values of the node scores calculated using Eq. (8). And the output of CategoryPool is obtained by concatenating the results of the two pools.

Moreover, an optimal network can be derived for each cross-validation iteration. By aggregating the adaptive scores of each brain region within these networks, the ultimate ranking of brain region importance can be determined.

IV. EXPERIMENTS AND RESULTS

To evaluate the performance of the proposed Temporal-BCGCN classification model, and to discuss the hemispheric lateralization abnormalities in SZ patients, this section is divided into three parts: 1) experimental implementation and setting, 2) comparison experiment, and 3) ablation experiment. To verify the robustness of the models, the Temporal-BCGCN and comparison models were cross-validated on two cohorts 10 times with five folds. Four-fold data were used for training; one-fold for testing, and six evaluation metrics to assess the performance of the model: accuracy (ACC), sensitivity (SEN), specificity (SPE), F1-Score, area under the receiver operating characteristic curve (AUROC), and area under the precision recall curve (AUPRC).

A. Experimental Implementation and Setting

Temporal-BCGCN was implemented using the PyTorch geometry and trained on an NVIDIA GeForce RTX 3080 Ti GPU. In this study, the Adam optimizer [43] and Binary cross entropy loss were used. The initial learning rate was set to 0.001, and the epoch number to 500. The window width W and sliding step s were set to divide the time series into m time slices, and then the node features and edge feature vectors were calculated for each time slice using the SPA and PCC methods, respectively. The final DSF-BrainNet comprised a set of graph nodes V and a set of edge features L.

In this study, the DSF-BrainNet was fed into a GCN classifier. The classifier primarily consisted of two convolutional layers and one pooling layer. The feature dimension of the convolutional layer was $d^0=d^1=m$. The number of nodes retained in the pooling layer was γ. The proportion of preserved brain regions in the left and right hemispheres was β_A and β_B. We designed an MLP with three layers ($10\times m$, $20\times m+1$, and two neurons per layer) that took the flattened graph as the input and predicted SZ versus HC.

Meanwhile, as suggested by Li *et al.* [44], Hancox-Li *et al.* [45], and Adebayo *et al.* [46], meaningful explanations are more likely to come from models with high classification accuracies. Therefore, we analyzed the experimental results

with better hyper-parameter configurations to explore hemispheric lateralization better.

Furthermore, to achieve optimal results, it is essential to debug W, s, β_A, and β_B. For W, we conducted tests and collected model outcomes for all settings in intervals of 10, spanning from 15 to 135. Additionally, in line with the configurations mentioned in Savva *et al.* [47], we set s to either 5 or 10. For β_A and β_B, we conducted tests and collected model outcomes for all settings in intervals of 0.1, spanning from 0 to 1. After debugging, we set $\gamma = 10$ to achieve an optimal accuracy of 83.62% on the COBRE dataset for $W = 45$, $s = 5$, and $\beta_A = 0.9 (\beta_B = 0.1)$ and achieved an optimal accuracy of 89.71% on the UCLA dataset for $W = 95$, $s = 10$, and $\beta_A = 0.7 (\beta_B = 0.3)$. We discussed the effects of W and s on the model in Section IV.C.2 and showed the results of the ablation of CategoryPool in Section IV.C.3.

B. Model Comparison

1) Comparison with the baseline model:

In this study, the baseline models based on sFC and dFC were used separately for comparison. There are five main types of baseline models.

a) Traditional machine learning (ML) algorithms for sFC: Principal component analysis (PCA) + support vector machine (SVM).

b) Traditional DL algorithms for sFC: Convolutional neural networks (CNN)

c) Advanced static brain network DL analysis method for the sFC: BrainGNN [44]

d) Advanced DL algorithms for dFC: GAT, UniMP

e) New dynamic brain network DL analysis methods for the dFC: HFCN [48] and CRNN [21].

Among the baseline models, including PCA + SVM, CNN, and BrainGNN, sFC was used. Specifically, sFC comprises the PCC values between the BOLD signals of all pairs of the 90 brain regions for each subject. For PCA + SVM and CNN, these sFC values form symmetric matrices representing each subject, serving as input data for the models. For BrainGNN, the feature vectors for each column of the symmetric matrix corresponded to the feature vectors of different nodes within the graph. The kernel function of the SVM classifier was a polynomial kernel function (linear) and PCA (cumulative percentage of variance = 0.9). CNN consisted of three composite convolutional layers and one fully connected classification layer. Each composite convolutional layer consisted of a convolutional and maximum pooling layer, and the size of the convolution kernel was set to 3×3. The model architecture of BrainGNN followed the setup described in the original paper.

The dFC was employed within the baseline models, including GAT, UniMP, HFCN, and CRNN. Specifically, we conducted a comprehensive exploration of the hyperparameters W and s for dFC, following an approach similar to that used in our model. For GAT and UniMP, the optimal hyperparameter settings for W and s were aligned with those of Temporal-BCGCN. For HFCN, the best hyperparameters for the COBRE and UCLA datasets were $W = 55$ when $s = 5$ and $W = 85$ when $s = 5$, respectively. For CRNN, the optimal hyperparameters for the COBRE and UCLA datasets were determined as $W = 45$ when $s = 10$ and $W = 75$ when $s = 5$, respectively. The GAT model consisted of two GATConv layers, one Top-kPool, and one fully connected classification layer. The output size of the fully connected classification layer was two. The UniMP model consisted of two UniMPConv layers, one Top-kPool layer, and one fully connected classification layer. The output size of the fully connected classification layer was two. The model architecture of HFCN, and CRNN followed the setup of the original paper.

As shown in Table I, the Temporal-BCGCN model slightly outperformed the baseline methods on the COBRE dataset and significantly outperformed the baseline methods on the UCLA dataset under a one-tailed two-sample t-test of $p < 0.05$. Specifically, the traditional ML algorithm PCA + SVM and the traditional DL algorithm CNN exhibited the worst results. The GAT, UniMP, HFCN, and CRNN models using dFC features performed slightly worse than BrainGNN using sFC features, whereas the temporal-BCGCN model proposed in this study outperformed BrainGNN. Therefore, although dFC contains more feature information than sFC, the performance of the model using dFC can be better than that of the advanced sFC model only if a suitable analysis framework is adopted. For example, DSF-BrainNet was proposed to build a topology for brain networks with synchronous temporal changes. TemporalConv was then proposed to maintain the synchronous time-varying features of the brain network during convolutional pooling. Maybe these reasons are why the Temporal-BCGCN model outperformed the other baseline models on both datasets. In conclusion, the proposed method is a superior tool for dynamic brain network analysis compared to other brain network analysis methods.

Moreover, on the COBRE dataset, our model achieved an AUROC of 78.87% and AUPRC of 76.44%. On the UCLA dataset, our model attained an AUROC of 86.14% and AUPRC of 85.78%. While our model's AUROC and AUPRC outperformed those of other baseline models, they both showed a decrease compared to ACC. This might be attributed to various factors, including the dataset size and quality. Consequently, in our future endeavors, we intend to perform experiments using more extensive and higher quality datasets.

2) Comparison with state-of-the-art methods

This study also compared the proposed model with the current state-of-the-art methods for SZ classification, as shown in Table II. In both datasets, Temporal-BCGCN exhibits better performance than the other state-of-the-art methods. The proposed model improves the ACC by at least 1.20% on the COBRE dataset and 6.22% on the UCLA dataset, significantly outperforming the other methods. These results demonstrate the rationality of the Temporal-BCGCN model and its superior representative learning capability.

C. Ablation Experiment

In this section, we report on the following ablation experiments to demonstrate the importance of the three key modules SPA, TemporalConv and CategoryPool.

1) Importance of SPA algorithm in DSF-BrainNet

In this study, the node features in DSF-BrainNet were replaced by the raw rs-fMRI sequences without reduction, and

TABLE I
COMPARISON OF THE CLASSIFICATION PERFORMANCE WITH THOSE OF DIFFERENT BASELINE MODELS

Dataset		COBRE (mean (std), %)						UCLA (mean (std), %)					
Classifiers	Type	ACC	SEN	SPE	F1-Score	AU-ROC	AU-PRC	ACC	SEN	SPE	F1-Score	AU-ROC	AU-PRC
PCA+SVM	sFC	78.27 (6.26)	77.84 (12.83)	79.19 (13.58)	76.04 (9.69)	66.93 (9.87)	62.24 (10.45)	80.56 (3.58)	82.42 (13.31)	78.28 (14.34)	80.26 (9.64)	74.19 (10.76)	73.31 (11.37)
CNN	sFC	77.89 (11.43)	79.36 (10.84)	77.24 (11.91)	74.54 (7.18)	65.57 (9.38)	63.01 (10.55)	79.34 (5.71)	76.07 (8.70)	81.15 (14.25)	75.56 (8.67)	72.27 (9.56)	72.65 (10.85)
BrainGNN	sFC	81.28 (8.57)	**83.45** (9.06)	79.10 (8.65)	79.86 (6.14)	75.19 (8.46)	72.26 (7.97)	84.93 (6.69)	86.53 (8.39)	82.46 (8.86)	83.38 (6.61)	80.43 (6.96)	80.29 (7.51)
GAT	dFC	80.82 (6.46)	81.55 (10.83)	81.86 (10.37)	78.38 (8.49)	72.84 (8.72)	69.46 (7.03)	80.97 (5.74)	83.84 (8.58)	79.98 (11.82)	80.58 (8.47)	74.82 (8.47)	74.44 (9.39)
UniMP	dFC	78.11 (7.24)	79.23 (13.68)	81.46 (12.79)	76.45 (10.74)	70.25 (9.35)	68.99 (9.47)	82.45 (6.25)	84.42 (9.39)	82.84 (11.75)	82.72 (6.82)	75.01 (8.42)	75.73 (8.95)
HFCN	dFC	80.83 (6.86)	77.64 (11.26)	83.72 (9.43)	77.84 (8.16)	70.44 (8.21)	68.34 (8.46)	82.84 (8.76)	79.39 (9.92)	85.31 (10.83)	79.11 (9.44)	75.15 (9.63)	74.07 (10.27)
CRNN	dFC	79.29 (5.35)	77.31 (9.55)	81.46 (11.36)	78.13 (8.03)	68.91 (7.26)	67.62 (7.48)	82.67 (7.58)	83.08 (9.85)	80.19 (10.12)	82.31 (8.18)	77.92 (8.31)	76.36 (9.09)
Proposed Method	dFC	**83.62** (4.27)	83.21 (7.32)	**84.07** (8.95)	**80.53** (4.71)	**78.87** (5.86)	**76.44** (6.45)	**89.71** (4.50)	**89.92** (8.51)	**89.56** (7.27)	**89.35** (5.39)	**86.14** (6.47)	**85.78** (6.95)

TABLE II
COMPARISON WITH STATE-OF-THE-ART METHODS

Methods	Datasets	Modality	HC/SZ Classification		
			ACC (%)	SEN (%)	SPE (%)
Zou *et al.* (2020) [49]	COBRE, NMorphCH	rs-fMRI	80.49	83.72	76.92
Ghosal *et al.* (2021) [50]	LIBD	fMRI, Genetic data	58.00	60.00	56.00
	BARI		73.00	66.00	83.00
Shi *et al.* (2021) [51]	COBRE	sMRI, fMRI	83.49	68.69	**93.75**
Cui *et al.* (2021) [52]	Clinical	sMRI	68.00	60.00	61.00
Wang *et al.* (2022) [9]	COBRE	sMRI, rs-fMRI	82.42	88.57	75.00
Sun *et al.* (2022) [53]	Clinical	sMRI	75.00	80.65	69.70
Proposed Method	COBRE	rs-fMRI	83.62	83.21	84.07
	UCLA		**89.71**	**89.92**	89.56

TABLE III
COMPARISON OF TEMPORALCONV WITH VARIOUS GRAPH CONVOLUTION STRATEGIES

Dataset	COBRE (mean (std), %)						UCLA (mean (std), %)					
Conv	ACC	SEN	SPE	F1-Score	AU-ROC	AU-PRC	ACC	SEN	SPE	F1-Score	AU-ROC	AU-PRC
ECConv	75.24 (5.36)	70.08 (16.37)	80.86 (11.87)	69.80 (8.13)	66.43 (8.73)	65.70 (10.02)	82.86 (6.40)	81.88 (10.90)	81.22 (9.74)	80.07 (7.11)	79.85 (7.96)	79.03 (8.24)
GATConv	81.43 (7.81)	82.19 (15.21)	82.58 (10.49)	78.97 (9.42)	72.01 (7.19)	69.59 (8.38)	81.72 (4.26)	84.76 (9.69)	80.65 (12.92)	81.79 (4.00)	78.62 (8.47)	77.58 (9.39)
UniMPConv	78.67 (5.86)	75.82 (14.39)	**86.45** (11.16)	73.36 (11.49)	71.86 (9.72)	70.25 (9.06)	83.71 (5.27)	85.55 (10.88)	83.61 (10.30)	83.29 (5.68)	81.26 (7.03)	80.80 (7.61)
TemporalConv (ours)	**83.62** (4.27)	**83.21** (7.32)	84.07 (8.95)	**80.53** (4.71)	**78.87** (5.86)	**76.44** (6.45)	**89.71** (4.50)	**89.92** (8.51)	**89.56** (7.27)	**89.35** (5.39)	**86.14** (6.47)	**85.78** (6.95)

TABLE IV
COMPARISON OF VARIOUS POOLING STRATEGIES BASED ON CATEGORYPOOL

Dataset	COBRE (mean (std), %)						UCLA (mean (std), %)					
Pooling	ACC	SEN	SPE	F1-Score	AU-ROC	AU-PRC	ACC	SEN	SPE	F1-Score	AU-ROC	AU-PRC
SortPool	79.62 (4.07)	69.59 (9.47)	**87.55** (6.61)	73.91 (6.11)	71.36 (5.91)	68.23 (5.63)	81.72 (6.03)	88.75 (12.09)	77.42 (12.79)	81.97 (6.56)	79.90 (8.03)	78.85 (7.64)
CategoryPool (Sort)	**80.19** (3.52)	**72.89** (8.75)	86.78 (7.51)	**75.55** (4.79)	**71.84** (6.74)	**69.77** (7.15)	**89.71** (4.41)	**92.85** (9.64)	**87.82** (9.07)	**89.11** (6.04)	**85.42** (7.82)	**84.61** (7.79)
SAGPool	79.05 (4.41)	66.02 (9.60)	90.02 (6.95)	72.50 (4.79)	70.91 (6.85)	69.62 (6.81)	83.43 (5.54)	85.36 (11.84)	84.41 (12.93)	82.76 (6.86)	80.93 (8.43)	80.12 (9.86)
CategoryPool (SAG)	**84.29** (4.15)	**74.75** (7.23)	**92.37** (9.19)	**79.98** (5.68)	**72.95** (6.38)	**70.16** (7.59)	**86.28** (3.89)	**88.50** (9.03)	**86.90** (11.21)	**85.74** (5.32)	**83.56** (8.27)	**82.33** (7.64)
Top-kPool	82.48 (3.79)	83.17 (8.64)	83.71 (8.20)	79.45 (5.71)	73.03 (5.45)	72.46 (6.40)	88.14 (5.20)	88.75 (8.07)	89.45 (8.34)	87.36 (5.90)	84.27 (6.58)	84.06 (6.30)
CategoryPool (Top-k)	**83.62** (4.27)	**83.21** (7.32)	**84.07** (8.95)	**80.53** (4.71)	**78.87** (5.86)	**76.44** (6.45)	**89.71** (4.50)	**89.92** (8.51)	**89.56** (7.27)	**89.35** (5.39)	**86.14** (6.47)	**85.78** (6.95)

the features after reduction using the PCA algorithm. It should be noted that both the raw rs-fMRI sequence and the reduction features of the SPA or PCA algorithms have temporal characteristics. As shown in Fig. 5, Temporal-BCGCN achieves the best classification ACC and F1-Score for both COBRE and UCLA when the graph node features are constructed using the SPA algorithm. The above results indicate that the dynamic synchronization feature constructed by DSF-BrainNet using the SPA algorithm is more conducive to training the Temporal-BCGCN model.

2) Superiority of TemporalConv

To demonstrate fully the difference in the effectiveness of ECConv and TemporalConv, we discuss the ACC of temporal-BCGCN networks based on ECConv and TemporalConv with different window widths W and sliding step s for the COBRE and UCLA datasets, respectively, as shown in Fig. 6. We also present the model results for ECConv, GATConv, UniMPConv, and TemporalConv under the optimal hyperparameter configuration in Table III.

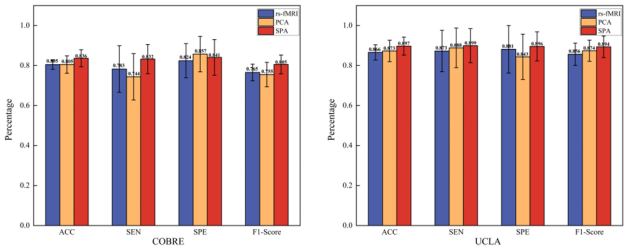

Fig. 5. SPA ablation comparison test results. rs-fMRI represents the graph node features as the original rs-fMRI signal sequence.

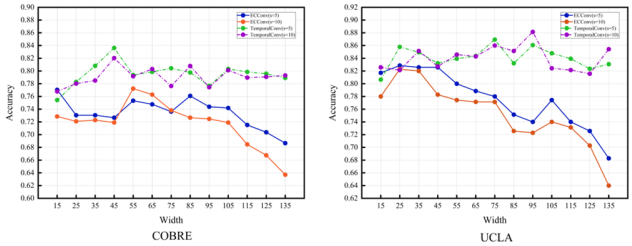

Fig. 6. ACC of Temporal-BCGCN models based on ECConv and TemporalConv with different window widths W and step sizes s.

As shown in Fig. 6, the ACC of the Temporal-BCGCN model with TemporalConv is higher than that with ECConv, and remains stable at a higher level than that of ECConv for different parameter settings. On the one hand, we can see that the window width W affects the model. Specifically, the window width governs the time scale on which the analysis is performed; ideally, it is long enough to accommodate the relatively slow frequencies of the BOLD signal and estimate dFC metrics with a sufficient signal-to-noise ratio, yet short enough to be sensitive to transient changes in network connectivity. However, the appropriate time scale for studying connectivity changes is presently an open question, and determining the optimal window width across a range of time scales is a common approach. On the other hand, the ACC of the ECConv-based model decreases as the window width W increases, apparently because ECConv convolves node and edge features in a fully connected manner, which results in imperfect exclusion of redundant information. Specifically, as W increases, more time slices overlap, and more redundant information is present in the node and edge vectors. However, ECConv feeds all edge vectors into a shared MLP for fully connected operation during convolutional message passing, and the adaptive parameters of this MLP are simultaneously applied to each component of each edge vector under different time slices. As the overlap between time slices increases, the redundancy of the data corresponding to the adaptive parameters increases further, resulting in a rapid decrease in the ability of ECConv to exclude redundant information. TemporalConv introduces an exclusive adaptive parameter $\omega^{\alpha}_{v_i,v_j}$ to adjust the current edge vector components dynamically, which to a certain extent eliminates the mutual interference between time slices and reduces the redundancy of information. In summary, TemporalConv can capture the implied brain dynamics more stably when excluding overlapping information between time slices.

As shown in Table III, TemporalConv exhibits the best overall performance on the COBRE and UCLA datasets under the optimal hyperparameter configuration. In particular, compared with the other models, all metrics are optimal and exceed 80%, except for the SPE of COBRE, which is lower than that of the UniMPConv model.

3) Superiority of CategoryPool

In this study, CategoryPool was used under the Top-kPool, SortPool [54] and SAGPool [55] pooling strategies. As shown in Table IV, the average accuracy of the models on the COBRE and UCLA datasets improved by 2.32% and 4.14%, respectively when each pooling method was nested using CategoryPool than when used alone. Simultaneously, the standard deviations of the models nested in CategoryPool converged, that is, the model quality was more stable. In summary, CategoryPool can improve the performance of various pooling strategies for specific problems. The reason for this improvement may be that, for rs-fMRI data, pooling the left and right hemispheres into different categories not only adapts to the characteristics of the data, but also captures some key features.

TABLE V
RELIABILITY EVALUATION BASED ON SRPBS DATASET

Classifiers	ACC	SEN	SPE	F1-Score	AU-ROC	AU-PRC
PCA+SVM	81.11 (4.88)	81.66 (9.77)	82.65 (10.99)	81.43 (9.72)	75.97 (9.68)	76.11 (9.35)
CNN	81.02 (5.31)	80.79 (8.57)	81.08 (9.54)	80.82 (8.56)	74.81 (9.35)	73.42 (9.64)
Brain GNN	86.60 (5.36)	**84.96** (7.44)	84.48 (7.72)	83.61 (6.77)	80.89 (6.47)	80.74 (6.65)
GAT	82.48 (5.42)	80.35 (8.31)	81.37 (9.68)	80.93 (8.41)	77.64 (9.15)	76.46 (9.22)
UniMP	83.95 (5.01)	85.53 (9.55)	82.43 (9.27)	82.85 (6.68)	78.42 (8.83)	79.18 (8.37)
HFCN	84.69 (7.45)	84.23 (8.65)	85.19 (9.52)	83.53 (9.28)	78.42 (8.73)	78.89 (9.15)
CRNN	84.23 (7.17)	83.81 (9.68)	85.76 (9.96)	83.53 (8.04)	78.84 (8.18)	79.36 (7.95)
Proposed Method	**87.10** (4.37)	83.73 (5.32)	**91.34** (7.25)	**85.00** (6.50)	**83.86** (6.68)	**82.87** (6.79)

D. Evaluation of model reliability

In order to better verify the reliability of this research method, this study further used the open dataset Strategic Research

Program for Brain Sciences (SRPBS) [56] to conduct supplementary tests. Specifically, we selected a total of 200 subjects from the Kyoto University TimTrio and Kyoto University Trio sites in this dataset, including all schizophrenia subjects totaling 92, and the first 108 healthy subjects in sample number order. Meanwhile, all the data were analyzed using the same preprocessing steps (Section II) and model implementation details (Section IV.A). In addition, the optimal performance of the model was obtained at $W=105$, $s=5$ and $\beta_A=0.8$, as shown in Table V. This result is nearly consistent with the main experimental conclusions in Section IV.B. Overall, our model has relative advantages in terms of reliability.

V. Discussion

To explore the lateralization abnormalities in the brain and its potential as disease biomarkers, CategoryPool was used and the brain was divided into two categories: left and right hemispheres. By adjusting β_A and β_B, we determined the proportion of preserved brain regions in each hemisphere. Finally, we discussed and analyzed the retained brain regions.

A. Existence of hemispheric lateralization abnormalities in SZ patients

To test whether there is abnormal lateralization in the brains of SZ patients, we first set the same weight for the left and right hemispheres, namely, $\beta_A=0.5(\beta_B=0.5)$. Next, during pool training, adaptive scores (according to Eq. (8)) were introduced to describe the importance of preserving the brain areas. Finally, the adaptive scores of the brain regions retained 10 times 5-fold cross-validations were accumulated and ranked; the top 10 brain regions are shown in Table VI, where the number of left hemisphere regions is seven in both datasets, significantly exceeding the right hemisphere. This finding also suggests that pathological changes in the left hemisphere of SZ patients may be more favorable for model classification training. In summary, there were more group-differentiated lesions in the left hemisphere of SZ patients. Moreover, brain regions that appeared simultaneously in both datasets were regarded as potential disease biomarkers (bold in Table VI), as shown in Fig. 7. Specifically, under the condition of equal status between the left and right hemispheres, the potential disease biomarkers identified in this study were located in the default-model network (DMN): precuneus (PCUN.R) and superior frontal gyrus medial (SFGmed.L), and visual network (VN): superior occipital gyrus (SOG.L) and fusiform gyrus (FFG.L).

B. Analysis of hemispheric lateralization abnormalities in SZ patients

To analyze further the abnormal lateralization of the left hemisphere in SZ patients, under the COBRE and UCLA datasets, the model achieved the highest accuracy when $\beta_A=0.9(\beta_B=0.1)$ and $\beta_A=0.7(\beta_B=0.3)$ (i.e., when it was more inclined to choose left brain features), respectively. The importance of the lesions in the brain regions corresponding to the above values is listed in Table VII (top 10). Under both datasets, the top 10 brain regions were located in the left hemi-

TABLE VI

Order of Relative Importance of Pathological TOP10 Brain Regions When β_A is Equal to 0.5

COBRE		UCLA	
ROI abbr	Brain Network	ROI abbr	Brain Network
SFGmed.L	DMN	**SFGmed.L**	DMN
PCUN.R	DMN	ITG.L	LN
LING.R	VN	**PCUN.R**	DMN
SOG.L	VN	CAL.L	VN
HIP.L	-	**FFG.L**	VN
STG.L	SMN	MTG.R	DMN
PreCG.L	DAN	SFGdor.R	DMN
LING.L	VN	ACG.L	DMN
FFG.L	VN	DCG.L	VAN
PCG.R	DMN	**SOG.L**	VN

DMN: default-model network, DAN: dorsal attention network, LN: limbic network, SMN: somatosensory network, VAN: ventral attention network, VN: visual network, -: not in the cortical network.

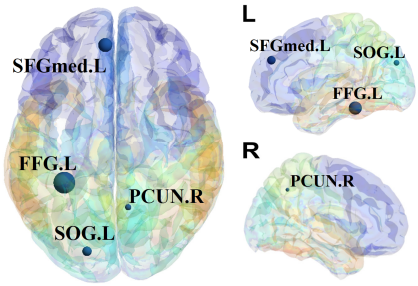

Fig. 7. Potential disease biomarkers under $\beta_A=0.5(\beta_B=0.5)$ (as shown in Table VI, the brain regions that appear in the importance sequences of both data sets are regarded as potential disease biomarkers).

TABLE VII

Order of Relative Importance of TOP10 Brain Regions Under Optimal Accuracy

COBRE		UCLA	
ROI abbr	Brain Network	ROI abbr	Brain Network
SOG.L	VN	LING.L	VN
FFG.L	VN	**SFGmed.L**	DMN
SFGmed.L	DMN	**IOG.L**	VN
TPOmid.L	LN	ACG.L	DMN
MOG.L	VN	**PreCG.L**	DAN
CAL.L	VN	**CAL.L**	VN
CUN.L	VN	MTG.L	DMN
IOG.L	VN	ITG.L	LN
STG.L	SMN	DCG.L	VAN
PreCG.L	DAN	PoCG.L	SMN

DMN: default-model network, DAN: dorsal attention network,LN: limbic network, SMN: somatosensory network, VAN: ventral attention network, VN: visual network, -: not in the cortical network.

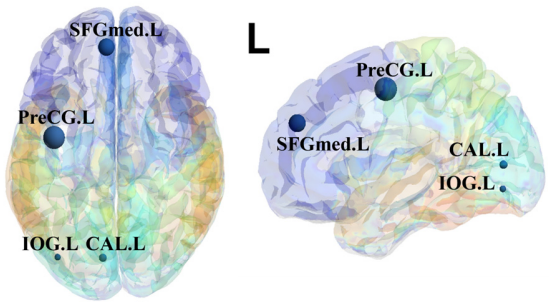

Fig. 8. Potential disease biomarkers with optimal accuracy (as shown in Table VII, the brain regions that appear in the important sequences of both data sets are regarded as potential disease biomarkers).

sphere, which further verified the conclusion drawn in Part A of this section. Additionally, brain regions that appeared simultaneously in both datasets were regarded as potential disease biomarkers (bold in Table VII), as shown in Fig. 8. Specifically, the potential disease biomarkers identified in this study was located in the VN: inferior occipital gyrus (IOG.L), calcarine fissure, and surrounding cortex (CAL.L); and dorsal attention network (DAN): precental gyrus (PreCG.L) and DMN (SFGmed.L) with the highest accuracy.

In summary, the results of the present study suggest that the left hemisphere of the brain in SZ patients seems to play a more critical role in classification prediction, which may suggest more severe lesions in the left hemisphere of the brain in SZ patients. Both Tables VI and VII show that accurate classification of SZ can be achieved based on the functional characteristics between the lower-order perceptual networks (VN and somatosensory network (SMN)) and the higher-order networks (DMN and limbic network (LN)). Indeed, it has been demonstrated that SZ involves many brain regions and is considered a widespread disconnected brain disease [57-59]. Additionally, the presence of functional abnormalities in DMN brain regions was shown to be associated with reduced interhemispheric sFC in the left intrahemisphere [7]. Xie *et al.* [27] found that the syrinx gyrus in DMN of SZ patients exhibited greater rs-fMRI signal variability and that this variability tended to be lateralized to the left.

More importantly, SFGmed.L, located in the DMN network, was labeled as an important potential disease biomarker in Tables VI and VII. Moreover, studies have identified the importance of this brain region in SZ. For example, Zhang *et al.* [28] observed significant hemispheric effects in 10 brain regions, including the precentral gyrus and medial part of the superior frontal gyrus, as well as the precentral gyrus and medial part of the superior frontal gyrus, which showed a left-leaning predominance in terms of regional efficiency. Pan *et al.* [60] found a significant reduction in connectivity at the whole-brain level in SZ patients whose working memory capacity was positively correlated with the strength of connections in SFGmed.L-SFGmed.R and SFGmed.L-Anterior cingulate and paracingulate gyri (ACG.R). Furthermore, consistent with the sensory gating hypothesis, the present study found significant predictive precision in the lower order perceptual system (occipital and primary sensorimotor cortex), reflecting dysregulation of the primary perceptual system in these two datasets [61]. Higher order brain regions, such as the prefrontal cortex, also showed good discrimination, which may be related to the executive dysfunction of the patients.

VI. Conclusion

In this study, a powerful and advanced model for dynamic brain network analysis, Temporal-BCGCN, was employed for classification and hemispheric lateralization analysis of SZ patients. The proposed model includes the following: (1) a unique dynamic functional brain network module DSF-BrainNet; (2) a revolutionary convolution method TemporalConv; and (3) a novel pooling strategy CategoryPool. The proposed model yielded average accuracies of 83.62% and 89.71% for the COBRE and UCLA datasets, respectively, exceeding those of the baseline models and other state-of-the-art methods. Meanwhile, the average accuracy of the model for SRPBS was 87.10%, which further verified the reliability of the model. This study showed that the lower order perceptual system and higher order network regions in the left hemisphere were more severely dysfunctional than those in the right hemisphere in SZ. This also confirmed the significance of the left medial superior frontal gyrus (SFGmed.L) in SZ. In conclusion, Temporal-BCGCN provides a promising means of restoring the spatiotemporal characteristics of cerebral neurodynamics and identifying the lateralization abnormalities of SZ patients. In future, we will develop more targeted DL functional modules based on the characteristics of medical image data to fully realize the potential of DL methods for medical image processing. Additionally, we will extend the use of TemporalConv to further explore patterns of abnormal activation in each time slice of the brain.

REFERENCES

[1] Y. Cui *et al.*, "Consistent brain structural abnormalities and multisite individualised classification of schizophrenia using deep neural networks," *Br. J. Psychiatry.*, vol. 221, no. 6, pp. 732-739, Dec. 2022.

[2] R. Salvador *et al.*, "Fingerprints as Predictors of Schizophrenia: A Deep Learning Study," *Schizophr. Bull.*, vol. 49, no. 3, pp. 738–745, May 2023.

[3] Y. Zhang, H. Zhang, L. Xiao, Y. Bai, V. D. Calhoun, and Y. P. Wang, "Multi-modal imaging genetics data fusion via a hypergraph-based manifold regularization: Application to schizophrenia study," *IEEE Trans. Med. Imaging*, vol. 41, no. 9, pp. 2263-2272, Sep. 2022.

[4] D. Alnæs *et al.*, "Brain heterogeneity in schizophrenia and its association with polygenic risk," *Jama Psychiatry*, vol. 76, no. 7, pp. 739-748, Jul. 2019.

[5] H. He *et al.*, "Trends in the incidence and DALYs of schizophrenia at the global, regional and national levels: results from the Global Burden of Disease Study 2017," *Epidemiol. Psychiatr. Sci.*, vol. 29, p. e91, Jan. 2020.

[6] B. Biswal, F. Z. Yetkin, V. M. Haughton, and J. S. Hyde, "Functional connectivity in the motor cortex of resting human brain using echo-planar MRI," *Magn. Reson. Med.*, vol. 34, no. 4, pp. 537-541, Oct. 1995.

[7] F. Zhu *et al.*, "Disrupted asymmetry of inter- and intra-hemispheric functional connectivity in patients with drug-naive, first-episode schizophrenia and their unaffected siblings," *Ebiomedicine*, vol. 36, pp. 429-435, Oct. 2018.

[8] Q. Zhu *et al.*, "Stacked topological preserving dynamic brain networks representation and classification," *IEEE Trans. Med. Imaging*, vol. 41, no. 11, pp. 3473-3484, Nov. 2022.

[9] T. Wang, A. Bezerianos, A. Cichocki, and J. Li, "Multikernel capsule network for schizophrenia identification," *IEEE Trans. Cybern.*, vol. 52, no. 6, pp. 4741-4750, Jun. 2022.

[10] Y. Liang, M. Long, P. Yang, T. Wang, J. Jiao and B. Lei, "Fused Brain Functional Connectivity Network and Edge-attention Graph Convolution Network for Fibromyalgia Syndrome Diagnosis," in *2023 45th Annual International Conference of the IEEE Engineering in Medicine & Biology Society*, 2023, pp. 1-5

[11] Q. Zuo, N. Zhong, Y. Pan, H. Wu, B. Lei and S. Wang, "Brain Structure-Function Fusing Representation Learning Using Adversarial Decomposed-VAE for Analyzing MCI," in *IEEE Transactions on Neural Systems and Rehabilitation Engineering*, vol. 31, pp. 4017-4028, 2023.

[12] X. Song et al., "Multicenter and Multichannel Pooling GCN for Early AD Diagnosis Based on Dual-Modality Fused Brain Network," in *IEEE Trans. Med. Imaging*, vol. 42, no. 2, pp. 354-367, Feb. 2023.

[13] V. D. Calhoun, R. Miller, G. Pearlson, and T. Adal, "The chronnectome: timevarying connectivity networks as the next frontier in fMRI data discovery," *Neuron*, vol. 84, no. 2, pp. 262-274, Oct. 2014.

[14] Y. Du, Z. Fu, and V. D. Calhoun, "Classification and prediction of brain disorders using functional connectivity: Promising but challenging," *Front. Neurosci.*, vol. 12, pp. 525, 2018.

[15] X. Zhang *et al.*, "Test-retest reliability of dynamic functional connectivity in naturalistic paradigm functional magnetic resonance imaging," *Hum. Brain Mapping*, vol. 43, no. 4, pp. 1463-1476, Mar. 2022.

[16] Z. Wang, *et al.*, "NDCN-Brain: An extensible dynamic functional brain network model," *Diagnostics*, vol. 12, no. 5, May 23, 2022.

[17] W. Yang, *et al.*, "Alterations of dynamic functional connectivity between visual and executive-control networks in schizophrenia," *Brain Imaging Behav.*, vol. 16, no. 3, pp. 1294-1302, Jun. 2022.

[18] M. Bahrami, *et al.*, "A mixed-modeling framework for whole-brain dynamic network analysis," *Netw. Neurosci.,* vol. 6, no. 2, pp. 591-613, Jun. 2022.

[19] Y. Li, J. Liu, Z. Tang, and B. Lei, "Deep spatial-temporal feature fusion from adaptive dynamic functional connectivity for MCI identification." *IEEE Trans. Med. Imaging*, vol. 39, no. 9, pp. 2818-2830, Sept. 2020.

[20] Y. Li, J. Liu, Y. Jiang, Y. Liu and B. Lei, "Virtual adversarial training-based deep feature aggregation network from dynamic effective connectivity for MCI identification." *IEEE Trans. Med. Imaging*, vol. 41, no. 1, pp. 237-251, Jan. 2022.

[21] K. Lin, *et al.*, "Convolutional recurrent neural network for dynamic functional MRI analysis and brain disease identification," *Front. Neurosci*., vol. 16, pp. 933660, 2022.

[22] J. P. Ramirez-Mahaluf *et al.*, "Dysconnectivity in schizophrenia revisited: Abnormal temporal organization of dynamic functional connectivity in patients with a first episode of psychosis," *Schizophr. Bull.*, Dec. 2022.

[23] D. Lei *et al.*, "Graph convolutional networks reveal network-level functional dysconnectivity in schizophrenia," *Schizophr. Bull*., vol. 48, no. 4, pp. 881-892, Jun. 2022.

[24] Q. Chang *et al.*, "Classification of first-episode schizophrenia, chronic schizophrenia and healthy control based on brain network of mismatch negativity by graph neural network," *IEEE Trans. Neural Syst. Rehabil. Eng.*, vol. 29, pp. 1784-1794, 2021.

[25] M. Simonovsky, and N. Komodakis, "Dynamic edge-conditioned filters in convolutional neural networks on graphs," in *IEEE Conference on Computer Vision and Pattern Recognition*, 2017, pp. 29-38.

[26] G. Berretz, O. T. Wolf, O. Güntürkün, and S. Ocklenburg, "Atypical lateralization in neurodevelopmental and psychiatric disorders: What is the role of stress?," *Cortex*, vol. 125, pp. 215-232, Apr. 2020.

[27] W. Xie *et al.*, "Functional brain lateralization in schizophrenia based on the variability of resting-state fMRI signal," *Prog. Neuro-psychopharmacol. Biol. Psychiatry*, vol. 86, pp. 114-121, Aug. 2018.

[28] Y. Zhang *et al.*, "Altered intra- and inter-hemispheric functional dysconnectivity in schizophrenia," *Brain Imaging. Behav.*, vol. 13, no. 5, pp. 1220-1235, Oct. 2019.

[29] H. Yuan, and S. Ji, "StructPool: Structured graph pooling via conditional random fields," in *International Conference on Learning Representations*, 2020.

[30] K. Gopinath, C. Desrosiers, and H. Lombaert, "Learnable pooling in graph convolutional networks for brain surface analysis," *IEEE Trans. Pattern Anal. Mach. Intell.*, vol. 44, no. 2, pp. 864-876, Feb. 2022.

[31] A.R. Mayer *et al.*, "Functional imaging of the hemodynamic sensory gating response in schizophrenia," *Hum. Brain Mapping*, vol. 34, no. 9, pp. 2302-2312, Sep. 2013.

[32] R. Bilder *et al.* (2020). UCLA Consortium for Neuropsychiatric Phenomics LA5c Study. *OpenNeuro.* [Dataset]. Available: https://openneuro.org/datasets/ds000030/versions/1.0.0

[33] C. Yan, X. Wang, X. Zuo, and Y. Zang, "DPABI: Data processing & analysis for (resting-state) brain imaging," *Neuroinformatics*, vol. 14, no. 3, pp. 339-351, 2016.

[34] K. J. Friston, S. Williams, R. Howard, R. S. Frackowiak, and R. Turner, "Movement-related effects in fMRI time-series," *Magn. Reson. Med.,* vol. 35, no. 3, pp. 346-355, Mar. 1996.

[35] G. J. Yang *et al.*, "Altered global brain signal in schizophrenia," *Proc. Natl. Acad. Sci. U. S. A.*, vol. 111, no. 20, pp. 7438-7443, May 2014.

[36] N. Tzourio-Mazoyer *et al.*, "Automated anatomical labeling of activations in SPM using a macroscopic anatomical parcellation of the MNIMRI single-subject brain," *NeuroImage*, vol. 15, no. 1, pp. 273 – 289, Jan. 2002.

[37] H. F. Hsueh, A. Guthke, T. Wöhling, and W. Nowak, "Diagnosis of model errors with a sliding time-window Bayesian analysis," 2021, *arXiv: 2107.09399*. [Online]. Available: https://arxiv.org/abs/2107.09399

[38] E. F. Guedes, A. M. da Silva Filho, and G. F. Zebende, "Detrended multiple cross-correlation coefficient with sliding windows approach," *Phys. A Stat. Mech. Appl*., vol. 574, 2021.

[39] L. Zhen *et al.*, "Simultaneous prediction for multiple source–loads based sliding window and convolutional neural network," *Energy Rep*., 2022.

[40] P. Velickovic *et al.*, "Graph attention networks," 2017, *arXiv:1710.10903*. [Online]. Available: https://arxiv.org/abs/1710.10903

[41] Y. Shi *et al.*, "Masked label prediction: Unified message passing model for semi-supervised classification," 2020, *arXiv:2009.03509*. [Online]. Available: https://arxiv.org/abs/2009.03509

[42] H. Gao, and S. Ji, "Graph U-Nets," *IEEE Trans. Pattern Anal. Mach. Intell.*, vol. 44, no. 9, pp. 4948-4960, Sep 2022.

[43] D. P. Kingma and J. Ba, "Adam: A method for stochastic optimization," 2014, *a*rXiv:1412.6980. [Online]. Available: https://arxiv.org/abs/1412.6980

[44] X. Li *et al.*, "BrainGNN: Interpretable brain graph neural network for fMRI analysis," *Med. Image. Anal.*, vol. 74, 2021.

[45] L. Hancox-Li, "Robustness in machine learning explanations: does it matter?" in *Proceedings of the 2020 Conference on Fairness, Accountability, and Transparency*, 2020.

[46] A. Julius, J. Gilmer, M. Muelly, Ian J. Goodfellow, M. Hardt, and B. Kim, "Sanity Checks for Saliency Maps." in *Neural Information Processing Systems*, 2018.

[47] A. D. Savva, G. D. Mitsis, and G. K. Matsopoulos, "Assessment of dynamic functional connectivity in resting-state fMRI using the sliding window technique," *Brain Behav.*, vol. 9, no. 4, Apr. 2019.

[48] C. Pan *et al.*, "Temporal-spatial dynamic functional connectivity analysis in schizophrenia classification," *Front. Neurosci.*, vol. 16, Aug. 2022.

[49] H. Zou, and J. Yang, "Multiple functional connectivity networks fusion for schizophrenia diagnosis," *Med. Biol. Eng. Comput.*, vol. 58, no. 8, pp. 1779–1790, 2020.

[50] S. Ghosal *et al.*, "A generative-discriminative framework that integrates imaging, genetic, and diagnosis into coupled low dimensional space," *NeuroImage*, vol. 238, 2021.

[51] D. Shi *et al.,* "Machine Learning of Schizophrenia Detection with Structural and Functional Neuroimaging," *Disease Markers*. 2021.

[52] L. B. Cui *et al.*, "Thalamus Radiomics-Based Disease Identification and Prediction of Early Treatment Response for Schizophrenia," *Front. Neurosci.*, vol. 15, Jul. 2021.

[53] H. Sun, G. Luo, S. Lui, X. Huang, J. Sweeney, and Q. Gong, "Morphological fingerprinting: Identifying patients with first-episode schizophrenia using auto-encoded morphological patterns," *Hum. Brain Mapping*, vol. 44, no. 2, pp. 779 – 789, Feb. 2023.

[54] M. Zhang, Z. Cui, M. Neumann, and Y. Chen, "An end-to-end deep learning architecture for graph classification," in *Proceedings of the AAAI Conference on Artificial Intelligence*, 2018, pp. 4438-4445.

[55] J. Lee, I. Lee, and J. Kang, "Self-attention graph pooling," 2019, *arXiv:1904.08082*. [Online]. Available: https://arxiv.org/abs/1904.08082

[56] S. C. Tanaka *et al.* "A multi-site, multi-disorder resting-state magnetic resonance image database." *Sci Data* 8, 227, 2021. Available: https://doi.org/10.1038/s41597-021-01004-8

[57] Y. Jiang *et al.*, "Characteristics of disrupted topological organization in white matter functional connectome in schizophrenia," *Psychol. Med*., vol. 52, no. 7, pp. 1333-1343, May 2022.

[58] X. Chen *et al.*, "Functional disconnection between the visual cortex and the sensorimotor cortex suggests a potential mechanism for self-disorder in schizophrenia," *Schizophr. Res*., vol. 166, no. 1-3, pp. 151-157, Aug. 2015.

[59] M. Valdés-Tovar *et al.*, "Insights into myelin dysfunction in schizophrenia and bipolar disorder," *World J. Psychiatry*, vol. 12, no. 2, pp. 264-285, Feb. 2022.

[60] Y. Pan *et al.*, "Abnormal network properties and fiber connections of DMN across major mental disorders: a probability tracing and graph theory study," *Cereb. Cortex*, vol. 32, no. 15, pp. 3127-3136, Jul. 2022.

[61] D. Dong *et al.*, "Reconfiguration of dynamic functional connectivity in sensory and perceptual system in schizophrenia," *Cereb. Cortex*, vol. 29, no. 8, pp. 3577-3589, Jul. 2019.